

## Selective Growth Inhibition of Cancer Cells with Doxorubicin-Loaded CB[7]-Modified Iron-Oxide Nanoparticles

F. Benyettou, H. Fahs, R. Elkharrag, R. A. Bilbeisi, B. Asma, R. Rezgui, L. Motte, M. Magzoub, J. Brandel, J.-C. Olsen, F. Piano, K. C. Gunsalus, C. Platas-Iglesias, and A. Trabolsi\*

### SUPPORTING INFORMATION

#### Table of Contents

<b>1. General Methods</b> .....	<b>2</b>
<b>2. Particle Synthesis</b> .....	<b>2</b>
2.1. Surface functionalization of NPs with CB[7] .....	2
2.2. Loading of CB[7]NPs with Dox.....	2
<b>3. NP Characterization</b> .....	<b>3</b>
3.1. Fourier transform infrared (FTIR) spectroscopy .....	3
3.2. HRTEM and PXRD .....	5
3.3. Thermogravimetric analysis (TGA).....	5
3.4. Dynamic light scattering (DLS) characterization.....	5
3.5. Magnetic property studies.....	7
3.6. Repsonse of Dox@CB[7]NPs to heating induced by an alternating magnetic field (AMF) .....	7
<b>4. Release studies</b> .....	<b>8</b>
4.1. Fluorescence emission spectroscopy.....	9
4.2. pH dependent release of Dox from CB[7]NPs.....	9
4.3. Glutathione dependent release of Dox from CB[7]NPs.....	9
4.4. Temperature dependent release of Dox from CB[7]NPs.....	9
4.5. Release of Dox from CB[7]NPs in neutral and acidic fetal bovine serum (FBS) .....	9
<b>5. Biological studies</b> .....	<b>10</b>
5.1. Cell culture .....	10
5.2. <i>In vitro</i> cellular uptake .....	10
5.3. Internalization pathway studies .....	11
5.4. Magnetic quantification of CB[7]NPs by HeLa cancer cells and HEK cells .....	14
5.5. <i>In vitro</i> cell viability assay.....	14
5.6. <i>In vitro</i> heating response of Dox@CB[7]NPs .....	17
5.7. <i>In vitro</i> hyperthermia treatment.....	17
5.8. Microscopy after chemotherapy and hyperthermia treatment.....	17
5.9. <i>C. elegans</i> maintenance.....	20
5.10. <i>C. elegans</i> growth, survival, embryonic lethality and reproduction assays .....	20
<b>6. Computational studies</b> .....	<b>23</b>
<b>7. Interaction of DOX with CB[7] in solution</b> .....	<b>25</b>
<b>8. Interaction of DOX with GSH in solution</b> .....	<b>26</b>
<b>9. References</b> .....	<b>30</b>

## 1. General Methods

All reagents were purchased from a commercial supplier (Sigma-Aldrich) and used without further purification. Nanopure water (conductivity of  $0.06 \mu\text{S cm}^{-1}$ ), obtained from a Millipore Gradient Elix-3/A10 system, was used to prepare the sample solutions. Iron concentration was deduced from UV-Visible absorption spectra recorded with an Agilent Technologies Cary 5000 Series UV-Vis-NIR Spectrophotometer in water at room temperature (298 K). Solutions were examined in 1 cm spectrofluorimetric quartz cells. The experimental error of the wavelength values was estimated to be  $\sim 1$  nm. Infrared spectra were recorded on an Agilent Technologies Cary 600 Series FTIR Spectrometer using the ATR mode. Thermogravimetric analyses were performed on a TA SDT Q600 device. Proton Nuclear magnetic resonance ( $^1\text{H}$  NMR) spectra were recorded at 298 K on a Bruker Advance 500 spectrometer with a working frequency of 500 MHz. Chemical shifts are reported in ppm relative to the signals corresponding to the residual non-deuterated solvent,  $\text{D}_2\text{O}$  ( $\delta = 4.97$ ). Magnetic properties of the nanoparticles were studied using a vibrating sample magnetometer, VSM (Quantum Design, Versalab). Emission spectra in water at room temperature were recorded on a Perkin Elmer LS55 Fluorescence Spectrometer using an excitation wavelength of 488 nm, which corresponds to the maximum absorption of Dox. Phase contrast and fluorescence images were observed on a Olympus FV1000MPE confocal scanning microscope. The nanoparticles were heated using magneTherm (NanoTherics), a device that allows magnetic fluid and nanoparticle hyperthermia testing. Dynamic light scattering (DLS) measurements were performed on a Malvern Zetasizer NanoSeries to obtain the size and  $\zeta$ -potential of the nanoparticles. Isothermal Titration Calorimetry experiments were carried out at 298K in water on a GE Healthcare Microcal ITC200 and the data processed with the Microcal Origin software (v.7.0) to obtain the thermodynamic parameters ( $\log K$ ,  $\Delta H$ ,  $\Delta S$ ) of the complexation of GSH by CB[7].

## 2. Particle Synthesis

### 2.1. Surface functionalization of NPs with CB[7]

Iron oxide nanoparticles, surface-functionalized with cucurbit[7]uril (CB[7]) were synthesized according to the procedure described in previous work.<sup>1</sup>

### 2.2. Loading of CB[7]NPs with Dox

CB[7]NPs ( $n_{\text{CB}[7]} = 1.3 \times 10^{-4}$  mol) and doxorubicin-HCl, *i.e.* Dox ( $1.5 \times 10^{-4}$  mol) were mixed in water ( $V = 3$  ml, CB[7]/Dox, 1:1.1) and stirred for 24 hours at room temperature and  $\text{pH} = 7$  to form inclusion complexes on the surface of NPs. Slow dialysis was used to remove excess Dox that was not interacting with the CB[7] macrocycles on the surface of the NPs. The brown precipitate,

Dox@CB[7]NPs, that was collected after dialysis was analyzed by FTIR, TGA and  $\zeta$ -potential measurements to confirm and quantify the adsorption of Dox to the CB[7]NPs.

### 3. NP Characterization

#### 3.1. Fourier transform infrared (FTIR) spectroscopy

Dox adsorption was confirmed and characterized using an Agilent Technologies Cary 600 Series FTIR Spectrometer.

The presence of a characteristic iron oxide band at  $\sim 600\text{ cm}^{-1}$  in the spectrum of Dox@CB[7]NPs demonstrates that the cores of the nanoparticles are preserved. The presence of Dox on the surface of CB[7]NPs, within CB[7], is confirmed by the appearance of new peaks between  $\sim 1600$  and  $900\text{ cm}^{-1}$  as illustrated in **Figure S1**. The shifting of the original CB[7]NPs peaks and the appearance of new peaks also confirms the interaction of Dox with the surface of CB[7]NPs. The spectrum of Dox@CB[7]NPs is not simply the sum of the various separate components, which confirms the presence of Dox within the CB[7]NPs.

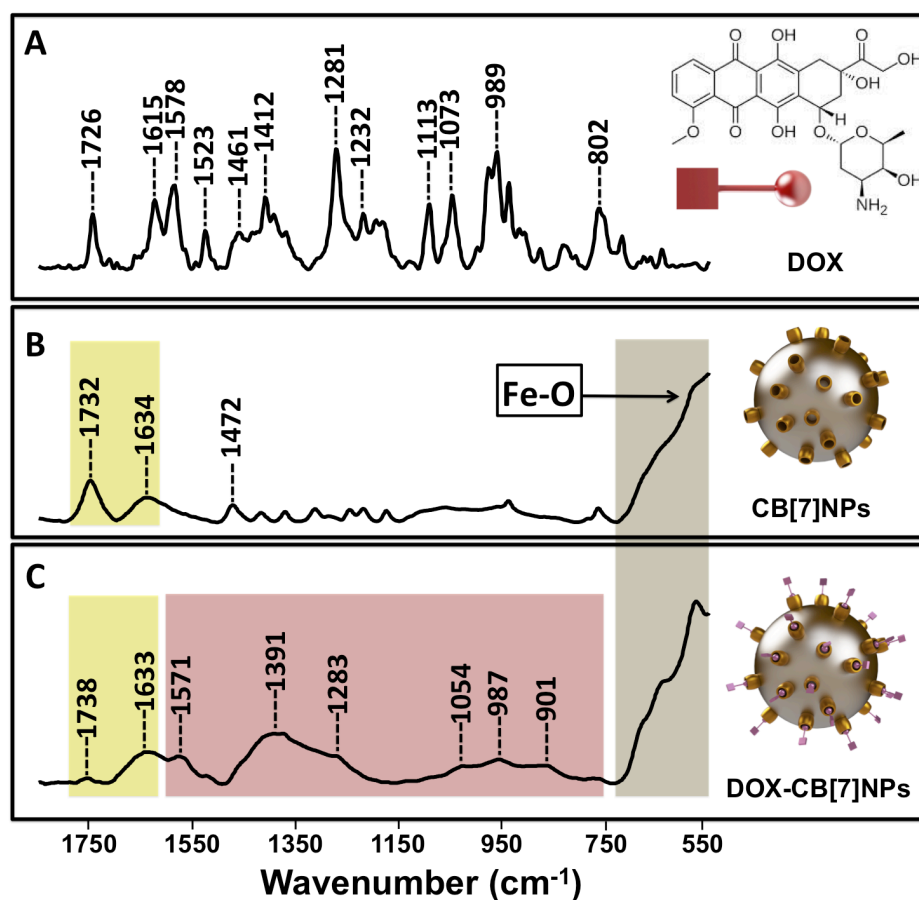


**Figure S1.** FTIR spectra of (A) free Dox, (B) CB[7]NPs and (C) Dox@CB[7]NPs.

**Figure S2** displays the FTIR spectra of CB[7]NPs at pH = 3, 7 and 12. These results clearly showed the presence of complexed CB[7] on the NPs surface all over the pH range.

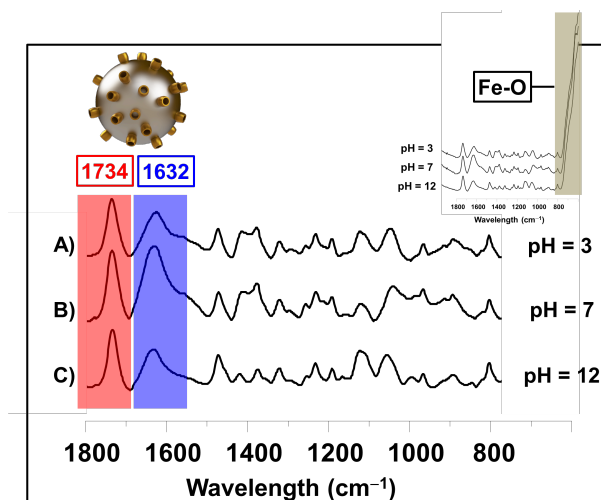


**Figure S2** FTIR spectra ( $800 - 1800 \text{ cm}^{-1}$ ) of CB[7]NPs at A) pH = 3 B) pH = 7 and C) pH = 12. Inset: FTIR spectra ( $600 - 1800 \text{ cm}^{-1}$ ) of CB[7]NPs at different pH that display the Fe-O bond used as a reference. The three spectra were normalized using the Fe-O bond.

### 3.2. High-Resolution TEM and Powder X-Ray Diffraction

Size and morphology of the nanoparticles were determined with a PHILIPS CM20 microscope operating at 200 kV. Samples were prepared on a carbon-coated copper grid. A drop of NP solution ( $[\text{Fe}] = 1.0 \times 10^{-5} \text{ M}$ ) was spotted on the grid and allowed to dry overnight. **Figure S3** shows surface functionalized with CB[7]. The particle size distribution was determined using a standard methodology.<sup>3</sup> In both cases the nanoparticles are  $8 \pm 1 \text{ nm}$  in diameter and present a spherical shape. The crystalline structure of the CB[7]NPs was characterized by powder X-ray diffraction (PXRD) (**Figure S3**). The reflections in the XRD patterns can be easily indexed with the inverse spinel structures of maghemite (ICDD PDF039-1346) indicating that the particles are consisting with  $\gamma\text{-Fe}_2\text{O}_3$  phase.

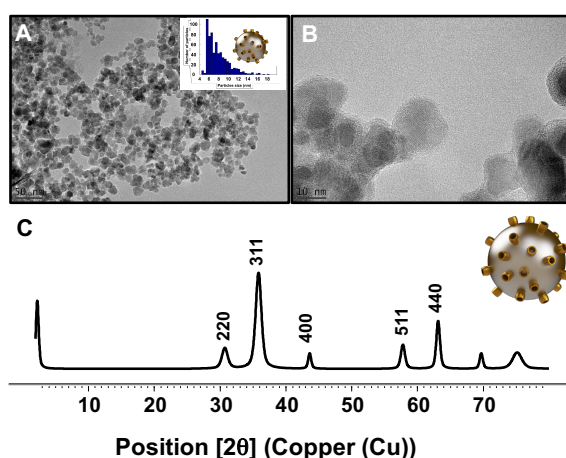


**Figure S3.** HRTEM images of CB[7]NPs (A, B). Histograms show the particles size distribution of CB[7]NPs. C) PXRD pattern of CB[7]NPs. Particles are consisting with  $\gamma\text{-Fe}_2\text{O}_3$  phase.

### 3.3. Thermogravimetric analysis (TGA)

The weight percentage of Dox interacting with CB[7] on the surface of CB[7]NPs was determined by TGA. Solid samples (10 mg) under N<sub>2</sub>(g) flux were characterized with a SDT Q600 TA Instruments analyzer at a heating rate of 5 °C/min over a temperature range of 35-700 °C. **Figure S4** presents the weight losses of CB[7]NPs before (black curve) and Dox@CB[7]NPs (red curve). The greater percentage loss that occurs when Dox@CB[7]NPs are heated is due to loss of Dox. These data are consistent with the successful loading of CB[7]NPs with Dox. The TGA analysis (**Table S1**) of Dox@CB[7]NPs shows a composition of 88.2 % iron oxide, 5.06 % of water, 4.14 % of CB[7] and 2.06 % of Dox corresponding to a 1:1 guest:host interaction (*i.e.* a 1:1 Dox:CB[7] interaction). The data suggest that twenty eight 1:1 Dox:CB[7] complexes are adsorbed to each NP.

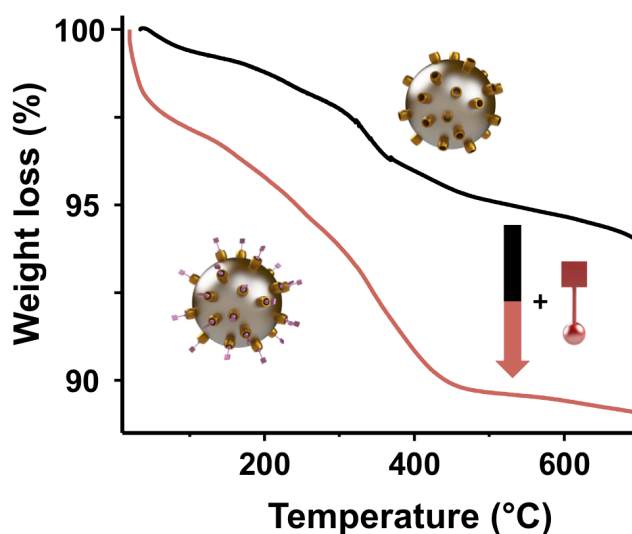


**Figure S4.** Thermo-gravimetric analysis of CB[7]NPs (black) and Dox@CB[7]NPs (red).

	Weight loss (%)	Mass in 1 g (g)	n in 1 g (mol)
$\gamma$ -Fe <sub>2</sub> O <sub>3</sub> (NPs)	88.2	0.88	$n_{\text{NP}} = 2.5 \times 10^{-7}$
CB[7]	4.14	0.04	$3.4 \times 10^{-5}$
Dox	2.06	0.02	$3.6 \times 10^{-5}$

**Table S1.** TGA calculations for Dox@CB[7]NPs.

### 3.4. Dynamic light scattering (DLS) characterization

DLS measurements were carried out on a Zetasizer Nano-ZS (Malvern Instruments) to determine the Zeta( $\zeta$ )-potential of the particles. All samples were analyzed at room temperature in water with diluted ferrofluid ([Fe] =  $1 \times 10^{-3}$  M).

At pH 7, the  $\zeta$ -potential of CB[7]NPs changes from +35 mV to -20 mV when Dox interacts with the CB[7]NPs (**Figure S5**). This change in surface charge remains sufficient to cause enough repulsion between Dox@CB[7]NPs to stabilize them. The isoelectric point also shifts from pH 8.9 to pH 3.7 upon Dox interaction. These changes in surface properties are also evidence of successful loading of the CB[7]NPs with Dox.

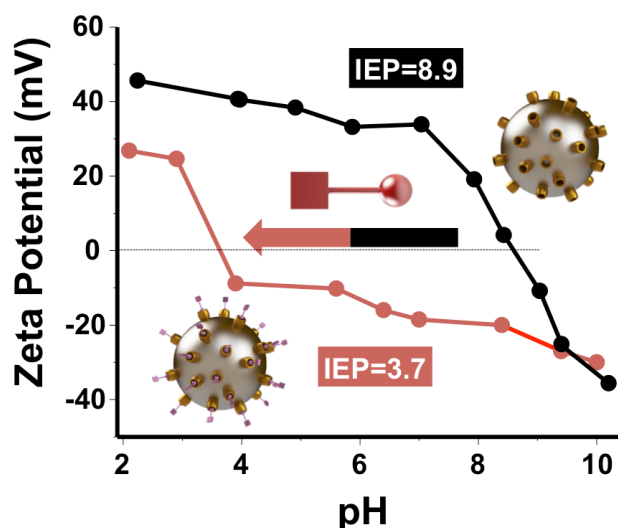


**Figure S5.** Zeta potential results for Dox@CB[7]NPs (red) and CB[7]NPs (black) as a function of pH.

To assess the stability of the Dox@CB[7]NPs as a function of pH, we used an automatic system that adjusts pH and measures the zeta potential simultaneously. **Figure S5** shows that the zeta potentials of Dox@CB[7]NPs and CB[7]NPs are different at pH 5 and at pH 7. In order, to confirm the release of the drug from Dox@CB[7]NPs, we measured their zeta potential at pH 5.4 after 5 minutes and 24 hours. After 24 hours, the zeta potential of the sample became the same as the zeta potential of CB[7]NPs, about -34.8 mV, a correspondence that indicated that complete release of the drug had been achieved.

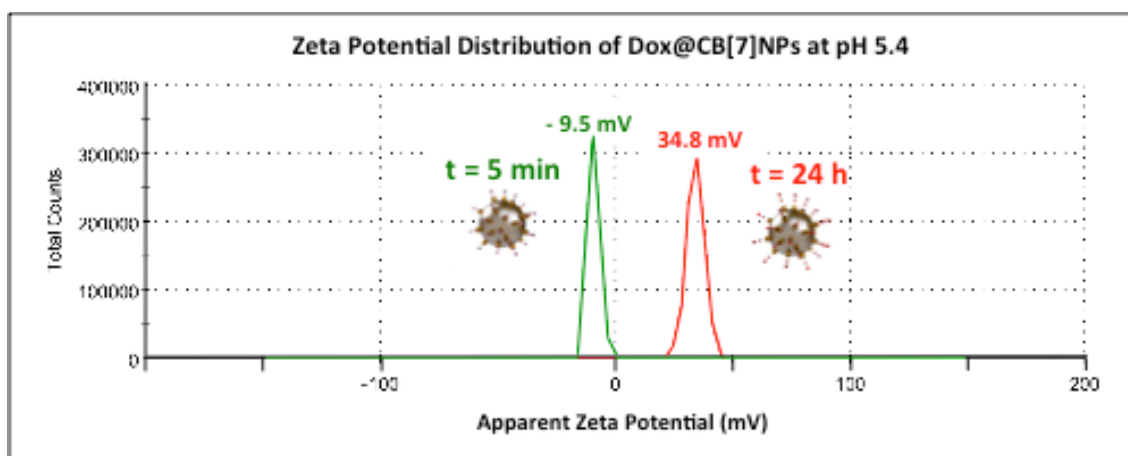


**Figure S6.** Zeta potential results of Dox@CB[7]NPs at pH 5.4 after 5 minutes and 24 hours.

### 3.5. Magnetic property studies

Magnetic properties of the CB[7]NPs and Dox@CB[7]NPs were studied using a vibrating sample magnetometer (VSM, Quantum Design, Versalab). The VSM measures the magnetization by cycling the applied field twice from  $-30$  to  $30$  kOe with a step rate of  $100 \text{ Oe.s}^{-1}$ . Measurements were performed on powdered samples at  $310 \text{ K}$ .

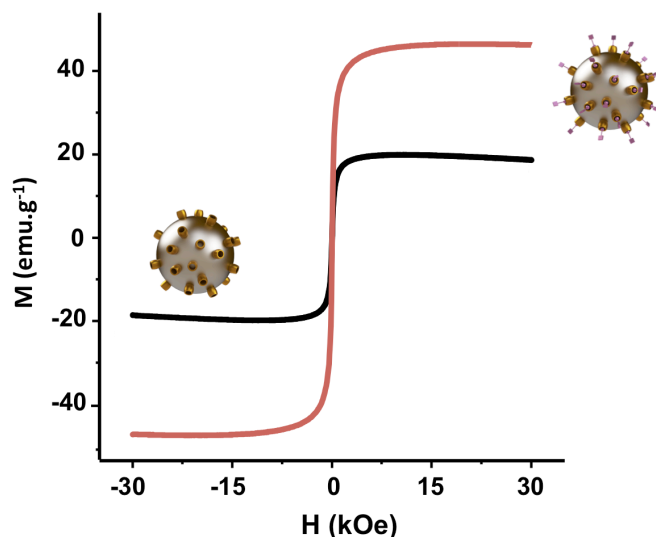


**Figure S7.** Field dependence of the magnetization of CB[7]NPs (black curve) and Dox@CB[7]NPs (red curve) at  $300 \text{ K}$ .

### 3.6. Response of Dox@CB[7]NPs to heating induced by an alternating magnetic field (AMF)

The effect of an alternating magnetic field (AMF) on the temperatures of solutions of Dox@CB[7]NPs, CB[7]NPs and uncoated NPs was investigated using a magneTherm. The device produces an alternating current (AC) magnetic field of frequency  $464 \text{ kHz}$  and a current of  $26.8 \text{ kAm}^{-1}$ . Samples ( $[\text{Iron}] = 0.2 \text{ M}$ ) of NPs, Dox@CB[7]NPs and CB[7]NPs were placed inside the magneTherm for two hours. The temperature of the samples was measured and recorded with respect to time using an external probe placed in the solution.

## 4. Release studies

### 4.1. Fluorescence emission spectroscopy

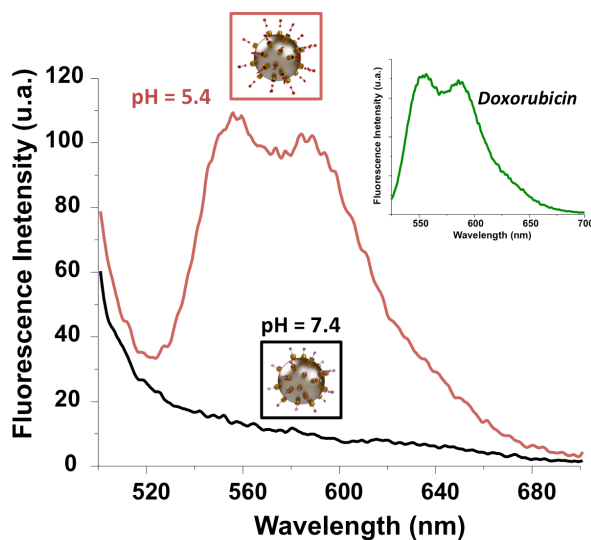


**Figure S8.** Fluorescence emission spectrum of Dox@CB[7]NPs in H<sub>2</sub>O at pH 7.4 and pH 5.4, 298 K and with  $\lambda_{ex} = 488$  nm.

Unloaded CB[7]NPs are not intrinsically fluorescent at the Dox-specific excitation wavelength of  $\lambda_{ex} = 488$  nm. At pH 7.4 and at  $\lambda_{ex} = 488$  nm, Dox@CB[7]NPs fluoresced less than an aqueous sample of free Dox of the same drug concentration. This indicates that fluorescence quenching occurs within the Dox@CB[7]NP construct. Such quenching can be attributed to electronic interactions between the excited dye molecules and the NPs, or to self-quenching of the dye on the surface of the particles where the effective concentration of the dye is relatively high.

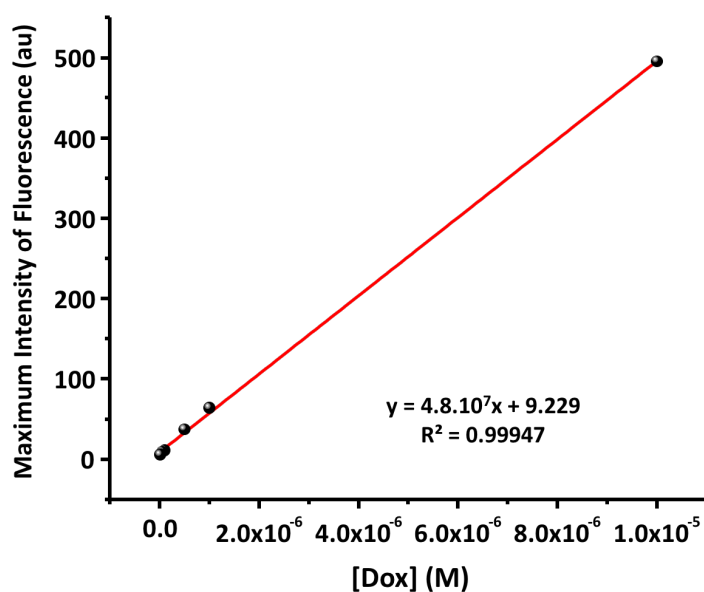


**Figure S9.** Calibration curve obtained by measuring the maximum fluorescence signal at different concentrations in Dox.

#### 4.2. pH dependent release of Dox from CB[7]NPs

The effect of pH on the release of Dox from Dox@CB[7]NPs was monitored in water buffered with PBS at pH = 7.4 and pH = 5.4 over time. The pH of the solutions was adjusted using a 1 M HCl<sub>(aq)</sub> solution. At regular intervals, solutions were centrifuged, supernatants were collected and the intensity of solution fluorescence was measured in comparison to a calibration curve.

#### 4.3. Glutathione dependent release of Dox from CB[7]NPs

The effect of competitive guest-triggered release of Dox from Dox@CB[7]NPs was investigated in PBS at pH = 7.4 and in the presence of glutathione (10 mM) over time. At regular intervals, solutions were centrifuged, supernatants were collected and the intensity of fluorescence was measured in comparison to a calibration curve.

#### 4.4. Temperature dependent release of Dox from CB[7]NPs

The effect of temperature on the release of Dox from CB[7]NPs was investigated by heating a Dox@CB[7]NP solution ([Dox] = 130 μM, [Iron] = 0.1 M) to final temperatures of 37 °C, 39 °C, 43 °C and 46 °C using Thermomixer comfort (1.5 mL). After two minutes of heating at a specific temperature, solutions were centrifuged and supernatants were collected and their fluorescence intensity was measured and compared to that of supernatant collected at 25 °C.

#### 4.5. Release of Dox from CB[7]NPs in neutral and acidic fetal bovine serum (FBS)

The stability of Dox@CB[7]NPs was assessed in the fetal bovine serum (FBS) by fluorescence spectroscopy. The fluorescence intensity of a sample of Dox@CB[7]NPs in FBS was measured for 5 days. Almost no release of the drug was observed during the first four days when the pH of the sample was at pH 7.4. This result confirms the stability of the Dox@CB[7]NPs under extracellular conditions and the lack of Dox leakage at physiological pH. When the pH of the sample was reduced to 5.4 by addition of HCl to mimic the conditions inside lysosomes, Dox release was immediately triggered, with complete release of achieved within three days of the pH adjustment.

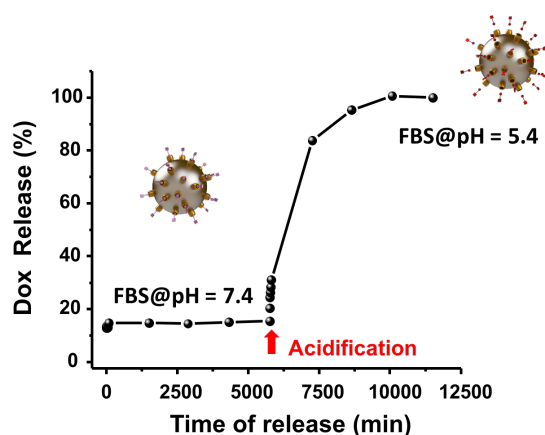


**Figure S10.** Dox release from Dox@CB[7]NPs in FBS after adjustment of the pH to 5.4 to mimic the conditions within lysosomes. Drug release was measured as a function of fluorescence emission.

## 5. Biological studies

### 5.1. Cell culture

Cervical epithelial cancer (HeLa; ATCC No. CCL-2), breast cancer (MCF-7, ATCC No. HTB-22) and non-cancer (Human Embryonic Kidney 293, HEK; ATCC No. CRL-1573) cells were cultured in Dulbecco's Modified Eagle's medium (DMEM), 10% fetal bovine serum (FBS), 1% penicillin/streptomycin and 20 mL L-glutamine at 5% CO<sub>2</sub> and 37 °C. Ovarian cancer (A2780, ECACC 93112519) and doxorubicin-resistant ovarian cancer cells (A2780/AD, ECACC 93112517) were cultured in Roswell Park Memorial Institute (RPMI)-1640 medium, 10% fetal bovine serum (FBS), 1% penicillin/streptomycin and 20 mL L-glutamine at 5% CO<sub>2</sub> and 37 °C.

### 5.2. *In vitro* cellular uptake

The intracellular uptake of Dox@CB[7]NPs was observed using confocal microscopy (Olympus FV1000MPE) measuring the fluorescence signal of Dox in HeLa cells. HeLa cells were seeded in Petri-dishes (~50,000 cell/mL) and incubated for 24 hours. After 24 hours, the medium was replaced with fresh DMEM (control), Dox ([Dox] = 10 μM in DMEM) or Dox@CB[7]NPs ([Dox] = 10 μM, [Iron] = 7 mM in DMEM) and the cells incubated for 2 hours. Cells were washed three times with phosphate buffered saline (PBS, Amresco Biotechnology grade). Confocal microscopy was used to compare treated cells versus control cells.

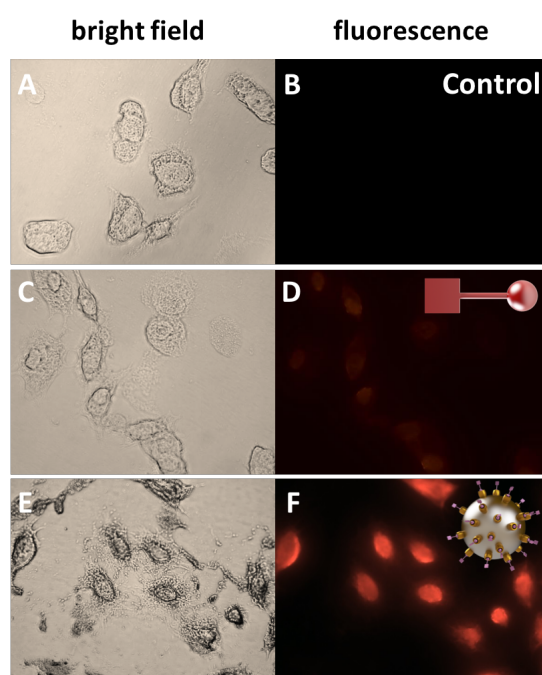


**Figure S11.** Bright field (A, C and E) and fluorescence (B, D and F) images of HeLa cells incubated for 2 hours with no additives (A, B) or with [Dox] = 10 μM, using free Dox (C, D) or Dox@CB[7]NPs (E, F). Red fluorescence at  $\lambda_{\text{ex}} = 488$  nm indicates Dox accumulation.

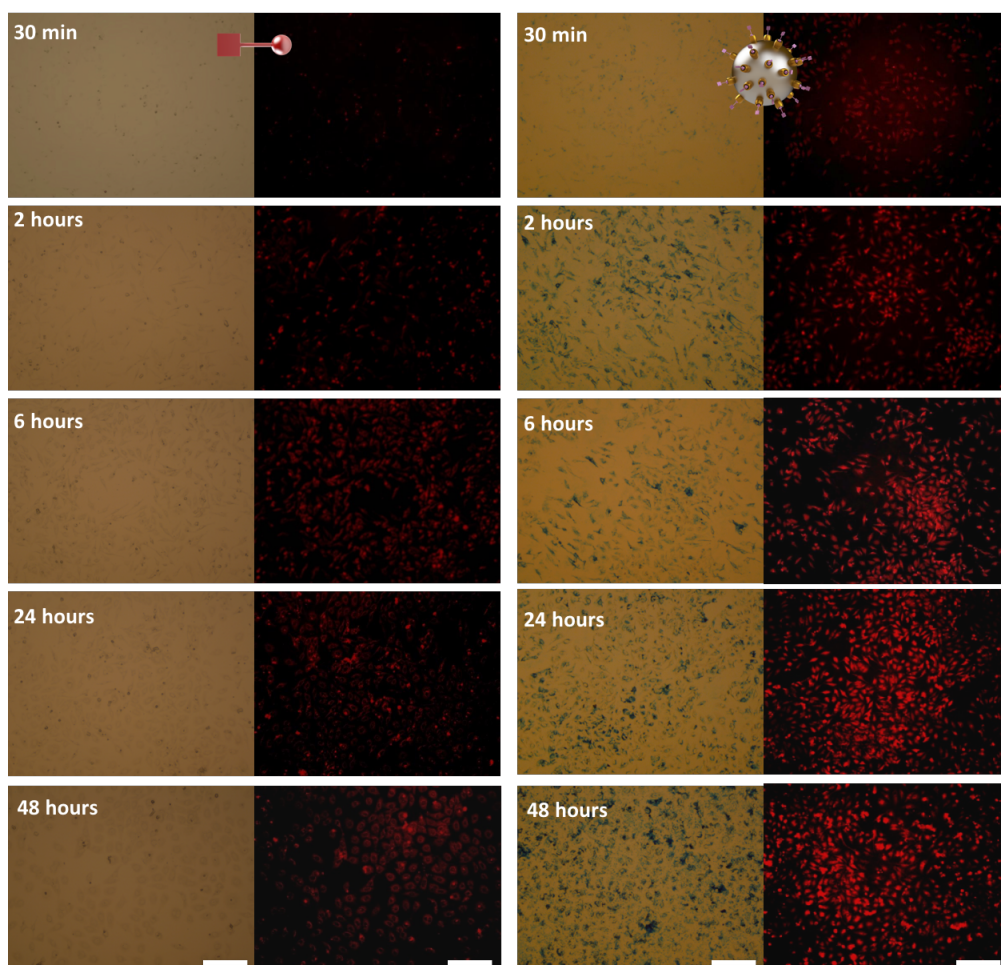


**Figure S12.** Bright field and fluorescence images of HeLa cells incubated various times (0, 30 min, and 2, 6, 24 and 48 hours) with  $[Dox] = 10 \mu M$ , using either free Dox (left column) or Dox@CB[7]NPs (right column). Red fluorescence at  $\lambda_{ex} = 488 \text{ nm}$  indicates Dox accumulation. Cellular iron content was determined *in situ* with a Prussian blue assay adapted for *in vitro* cell studies.

### 5.3 Internalization pathway studies

HeLa cells were seeded in Petri-dishes ( $\sim 50,000 \text{ cell/mL}$ ) and incubated for 24 hours. After 24 hours, 5 Petri-dishes of HeLa cells were incubated with one different endocytic inhibitor each: methyl- $\beta$ -cyclodextrin (MBCD), filipin (FLP), amiloride (AMI), ammonium chloride (AMCL), for 30 min prior to Dox@CB[7]NPs addition for 2 h ( $[Dox] = 10 \mu M$ ,  $[Iron] = 7 \text{ mM}$  in DMEM). As controls, 3 Petri-dishes of cells were treated with no additives (control), Dox ( $[Dox] = 10 \mu M$  in DMEM) or Dox@CB[7]NPs ( $[Dox] = 10 \mu M$ ,  $[Iron] = 7 \text{ mM}$  in DMEM) and incubated for 2 hours. Cells were washed 3 times with PBS and confocal microscopy was used to quantify Dox accumulation in cells.

**Table S2** summarizes the endocytotic inhibitor concentrations used:

Endocytic Inhibitor	Concentration ( $\mu\text{M}$ )
Cloroquine (CQN)	75
Methyl-B-Cyclodextrin (MBCD)	10
Filipin (FLP)	4.6
Cytochalasin (CLN)	20
Chlorpromazine (CPZ)	10

**Table S2.** Concentrations of endocytic inhibitors used in this study.

Cell viability tests were also performed to determine the toxicity of the inhibitors at the concentrations used. **Figure S11** shows that cell death was negligible for the initial concentrations used and increased only at 5- and 10-fold concentrations.

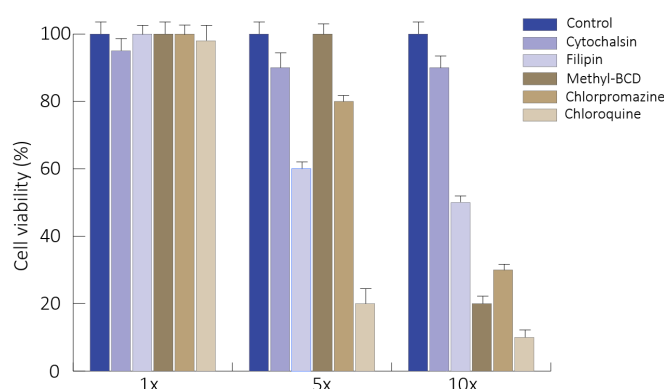


**Figure S13.** Viability of cells treated with endocytic inhibitors as measured with CellTiter-Blue®. Error bars represent standard deviations of triplicate measurements.

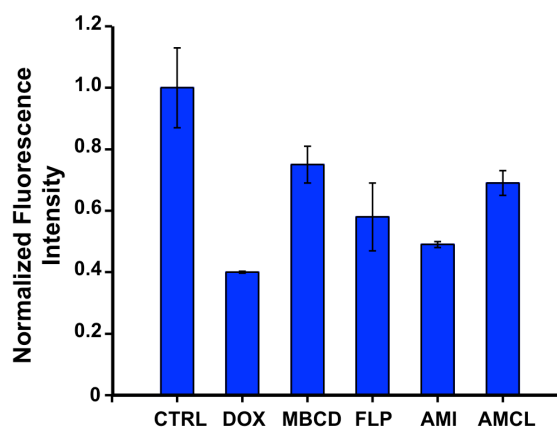


**Figure S14.** Effect of endocytotic inhibitors on cellular uptake of Dox@CB[7]NPs into HeLa cells. Left to right, the first two blue bars indicate the normalized fluorescence of cells incubated for 2 h with Dox@CB[7]NPs (CTRL) or Dox alone (DOX). The other bars indicate the normalized fluorescence of cells incubated for 2 h with Dox@CB[7]NPs and either methyl- $\beta$ -cyclodextrin (MBCD), filipin (FLP), amiloride (AMI) or ammonium chloride (AMCL). MBCD, FLP, AMI and AMCL are inhibitors of lipid raft synthesis, caveolin-dependent endocytosis, macropinocytosis and endosome acidification, respectively. Error bars represent standard deviations of triplicate measurements.

#### 5.4. Magnetic quantification of CB[7]NPs by HeLa cancer cells and HEK cells.

The absorbed amount of CB[7]NPs by HeLa cancer cells and HEK cells was determined using magnetic detection (MIAttek reader) based on the non-linearity of the materials' magnetization.<sup>2</sup> The MIAttek signal is proportional to the amount of magnetic particles and is very sensitive. This allows the detection of nanograms of superparamagnetic materials. The mean number of CB[7]NPs /cell (**Figure S14**) were obtained by dividing the total amount of iron measured with MIAttek by the number of cells. Biological samples exhibit only diamagnetism, a linear magnetic behavior, which does not disturb nonlinear magnetization measurement. As can be seen in **Figure 14**, the amount of iron loaded in the cells increased with the time reaching a plateau after 24 hours in HeLa cancer cells.

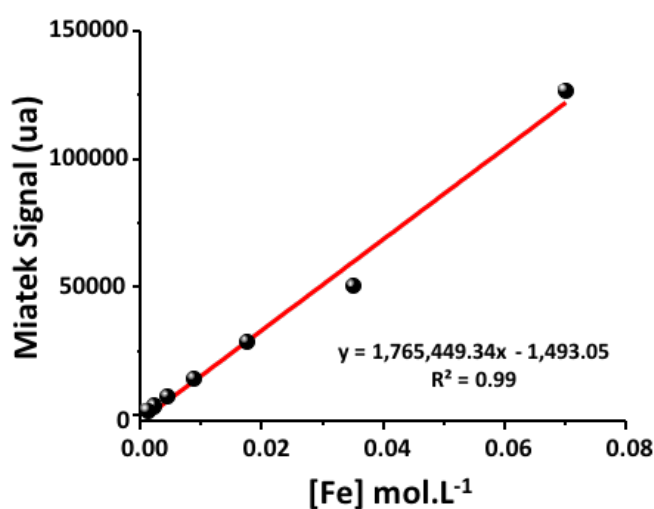


**Figure S15.** Calibration curve obtained by measuring the MiAttek signal of CB[7]NPs at different concentrations in iron.

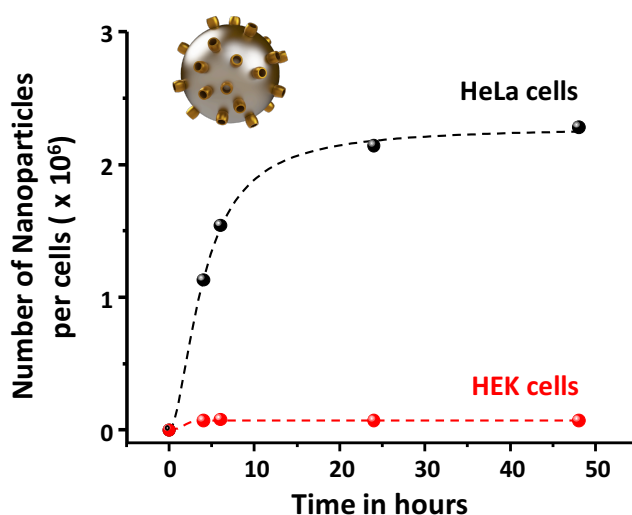


**Figure S16.** Amount of internalized CB[7]NPs in HeLa cancer cells versus HEK cells overtime ([Fe] = 300  $\mu$ M).

### 5.5. *In vitro* cell viability assay

Cell viability was assessed using CellTiter-Blue® Cell Viability assay (CTB, Promega). The assay measures the metabolic reduction of a non-fluorescent compound, resazurin, into a fluorescent product, resofurin, in living cells. As non-viable cells rapidly lose their metabolic activity, the amount of the resofurin product can be used to estimate the number of viable cells following treatment. Once produced, resofurin is released from living cells into the surrounding medium. Thus the fluorescence intensity of the medium is proportional to the number of viable cells present.

To determine the anti-proliferative properties and effectiveness of Dox@CB[7]NPs for Dox delivery, inhibition of HeLa, A2780, A2780/AD, MCF-7 and HEK-293 cell growth by Dox@CB[7]NPs versus free Dox was studied as well as the free-drug vehicle, CB[7]NPs.

96-well plates were seeded with cells (~5,000 cells per well in 100µL of DMEM) and incubated at 37 °C for 24 hours. The medium was removed and replaced with fresh DMEM (control) or various concentrations of Dox or Dox@CB[7]NPs (up to 100 µM in Dox) and incubated at 37 °C for 48 hours. Thereafter, cells were washed with PBS and incubated with 20 µL of CTB per well for 6 hours at 37 °C. The fluorescence of the resofurin product ( $\lambda_{ex/em}$  560/620) was measured. Untreated wells were used as control.

The percentage of cell viability and inhibition were calculated using the following formula:

$$\text{Viability (\%)} = [(F_{\text{treated}} - F_{\text{blank}}) / (F_{\text{control}} - F_{\text{blank}})] \times 100$$

$$\text{Inhibition (\%)} = 100 - \text{viability (\%)}$$

From the curves we deduced the concentration of Dox that caused a 50% decrease in cell growth ( $IC_{50}$ ).

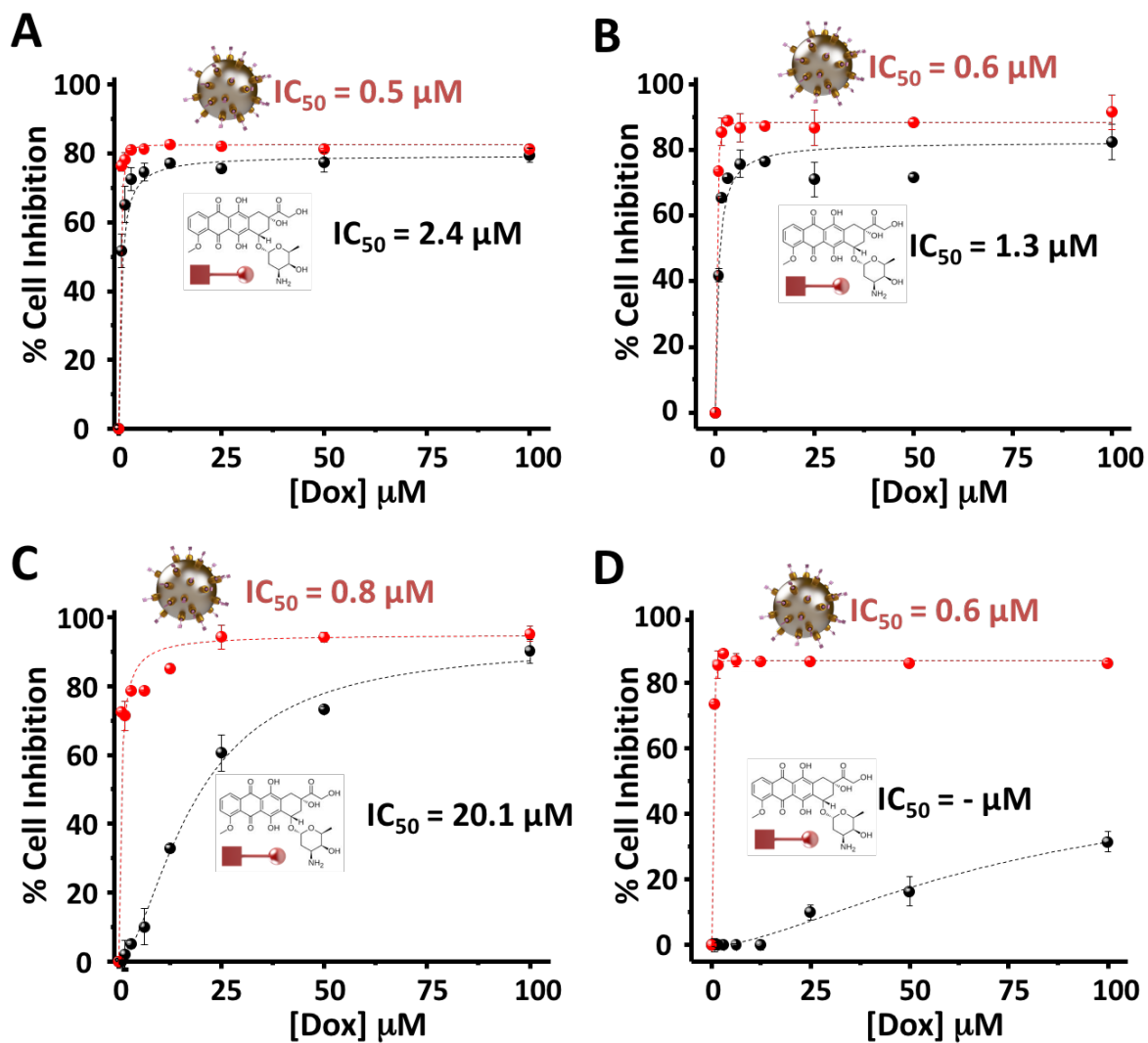


**Figure S17.** Cell Inhibition of A) HeLa, B) MCF-7, C) A2780 and D) Doxorubicin-resistant A2780 cells after 48 h incubation with Dox (dashed black curve) or Dox@CB[7]NPs (dashed red curve) plotted against concentration of Dox. Error bars represent standard deviations of triplicate measurements.

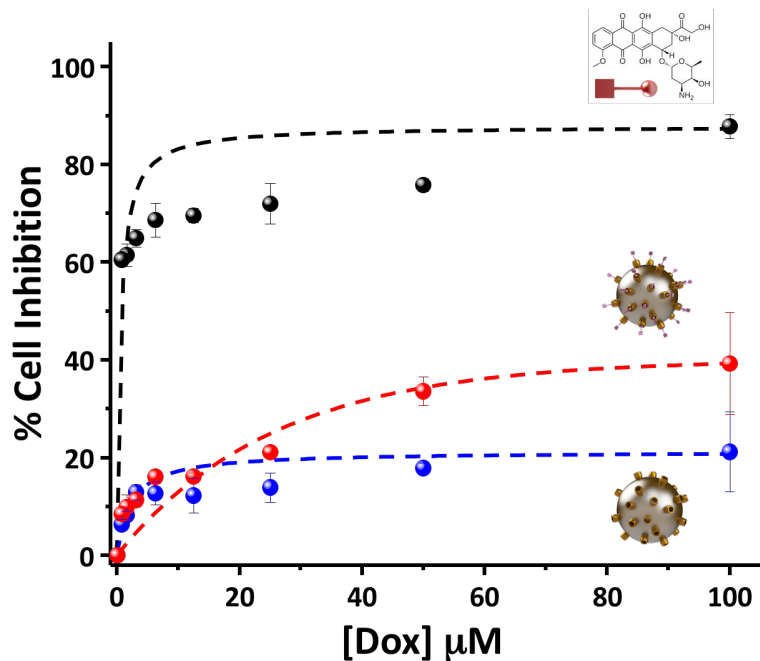


**Figure S18.** HEK inhibition of after 48 h plotted against concentration of free Dox (black), CB[7]NPs (blue) and Dox@CB[7]NPs (red). Error bars represent standard deviations of triplicate measurements.

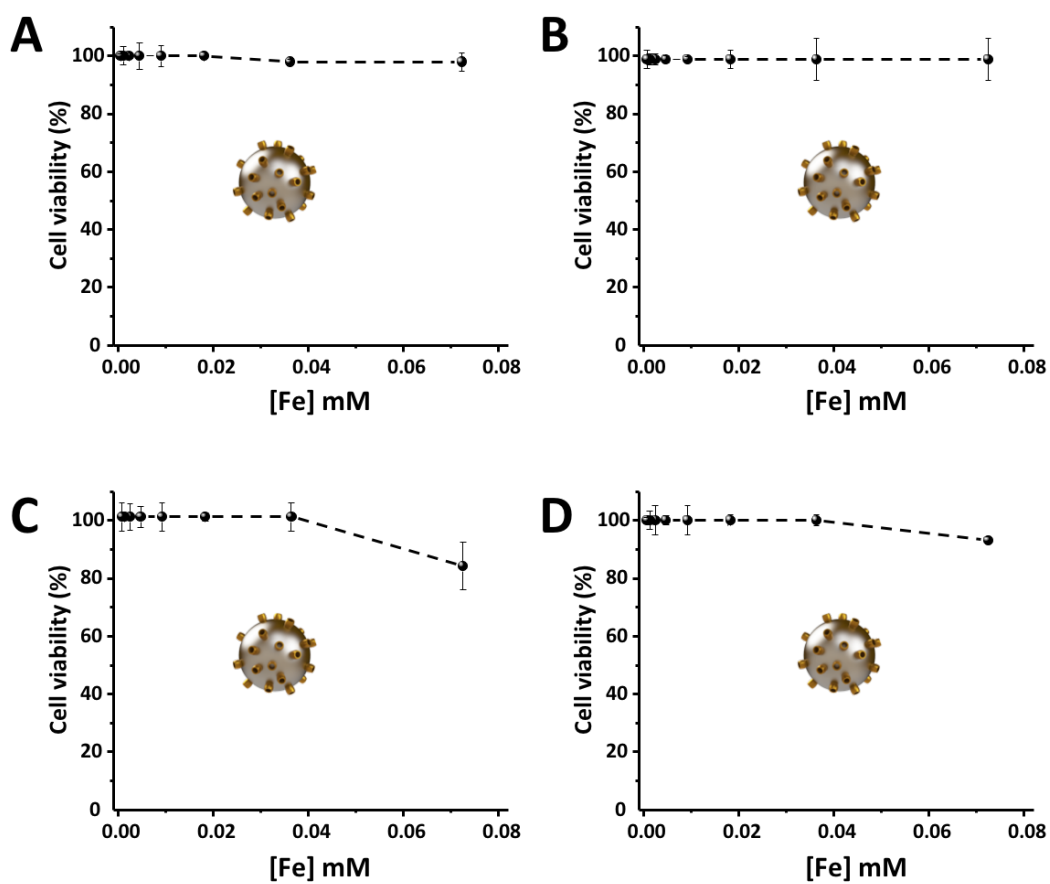


**Figure 19.** Cell Viability after 48 h incubation of A) HeLa, B) MCF-7, C) A2780 and D) Doxorubicin-resistant A2780 cells with CB[7]NPs plotted against concentration of iron. Error bars represent standard deviations of triplicate measurements.

### 5.6. *In vitro* heating response of Dox@CB[7]NPs

*In vitro* heat response of Dox@CB[7]NPs was studied by incubating HeLa cells with Dox@CB[7]NPs and subjecting the sample to magnetic hyperthermia using AMF (frequency = 464 kHz, current = 26.8 kAm<sup>-1</sup>). HeLa cells were seeded in 2 Petri-dishes (~50,000 cell/mL) and incubated for 24 hours. After 24 hours, the medium was replaced with fresh DMEM (control), or Dox@CB[7]NPs ([Dox] = 10 μM, [Iron]= 7 mM in DMEM) and incubate for 2 hours. Cells were washed three times with PBS and fresh DMEM was added to the petri-dishes. Cells were subjected to AMF for 30 minutes. The temperature increase of the cells during treatment was recorded using an external probe placed in the medium.

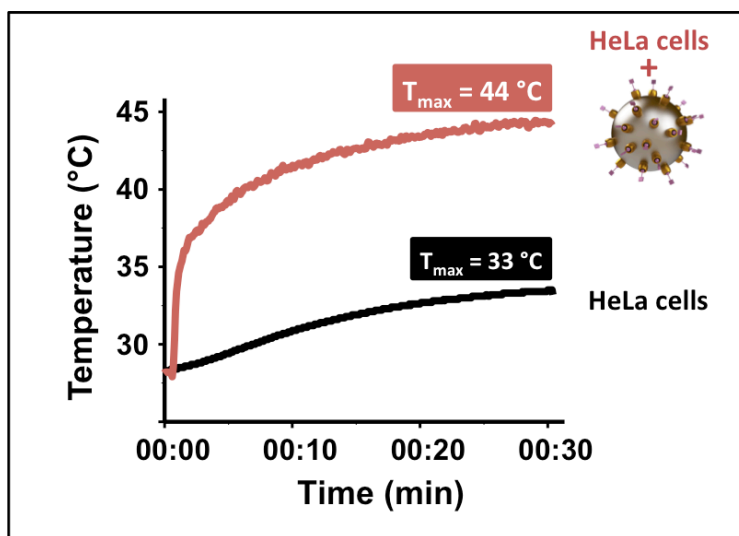


**Figure S20.** Temperature of the cells during 30 minutes of AMF application (frequency = 464 kHz, current = 26.8 kAm<sup>-1</sup>, [Dox] = 10 μM) to HeLa cells (black curve) and HeLa cells incubated for two hours with Dox@CB[7]NPs (red curve).

### 5.7. *In vitro* hyperthermia treatment

Viability tests were performed to investigate the combined effect of both hyperthermia and chemotherapy treatments on HeLa cells. Petri-dishes were seeded with HeLa cells (~50,000 cells/mL) and incubated at 37 °C for 24 hours. Cells were separated into four groups and incubated for two hours with cell-medium alone (control), free Dox ([Dox] = 10 μM), CB[7]NPs ([Iron]= 7 mM) or Dox@CB[7]NPs ([Dox] = 10 μM, [Iron]= 7 mM). A sample from each treatment group was then subjected to an AMF (frequency = 464 kHz, current = 26.8 kAm<sup>-1</sup>) for one hour to induce hyperthermia. The viability of unheated samples was measured immediately after incubation and 18 hours after incubation. The viability of heated samples was measured immediately after AMF removal and 18 hours after AMF removal. For cell viability studies, 200 μL CTB reagent per 1 mL of DMEM was added to each petri-dish which were incubated for six hours prior to fluorescence reading.

### 5.8. Microscopy after chemotherapy and hyperthermia treatment

To assess the changes in cell morphology after AMF sessions, HeLa cells were seeded in 6 Petri-dishes (~50,000 cell/mL) and incubated for 24 hours. After 24 hours, the medium was replaced with

fresh DMEM (control), Dox ([Dox] = 10  $\mu$ M), Dox@CB[7]NPs ([Dox] = 10  $\mu$ M, [Iron]= 7 mM in DMEM) and cells were incubated for 2 hours. Cells were washed three times with PBS and fresh DMEM was added to the petri-dishes. One petri dish of each group was subjected to one hour AMF (frequency = 464 kHz, current = 26.8 kAm<sup>-1</sup>). Cells were washed three times with PBS and fixed with 1 ml of a solution of formaldehyde (10% v/v) during one minute. Fixed cells were dried at room temperature overnight in the dark to prevent Dox photodegradation. Optical microscopy was used to compare changes in the morphology of treated cells compared to control.

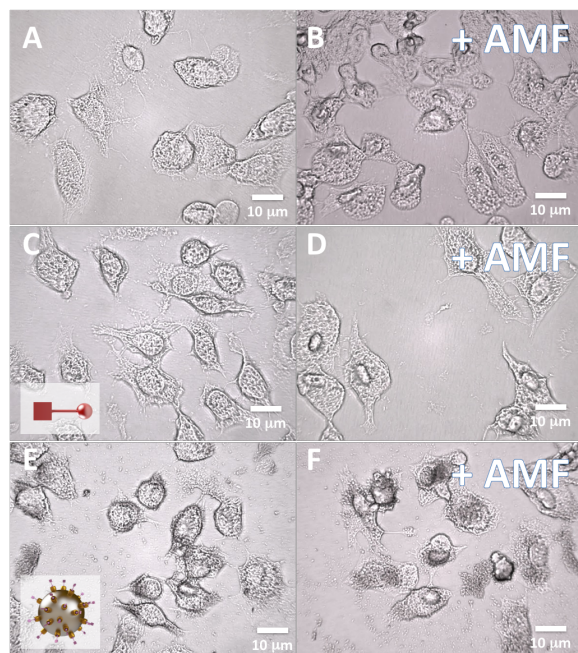


**Figure S21.** Optical images of HeLa cells before (B, D, F) and after (C, E, G) AMF-induced hyperthermia. Cells were exposed to the following conditions for two hours: no treatment (B, C), Dox incubation (D, E), or Dox@CB[7]NP incubation (F, G).

### 5.9. *C. elegans* maintenance

*C. elegans* wild-type strain N2 was maintained on NGM (Nematode Growth Medium) agar plates with *Escherichia coli* strain OP50 as food source and incubated in the dark at 20°C.<sup>3</sup> L1 and L4 worms were starved for 48 hours and 4 hours respectively, then supplemented with 100  $\mu$ L of intact or nanocoated bacteria. *E. coli* bacteria were prepared as described earlier.<sup>4</sup> Single bacterial colonies cultured overnight in LB medium at 37°C were harvested and washed with water. 300  $\mu$ L were aliquoted in microcentrifuge tubes containing 1 mL of CB[7]NPs or Dox@CB[7]NPs at defined iron concentration (10 mg/L, 100 mg/L and 500 mg/L) and vortexed for 10 minutes. Magnetized cells were then separated from unbound nanoparticles by centrifugation and washed with water. 100  $\mu$ L of different preparations were seeded on 6- or 12-well NGM agar plates with worms.

### 5.10. *C. elegans* growth, survival, embryonic lethality and reproduction assays

Each experiment was performed independently three times for each condition, with multiple replicates as indicated below. All assays were performed at 20°C on 6-well agar plates supplemented with fresh bacterial preparations (with or without nanoparticles). To assay larval growth, 30 L1 were monitored for three days and scored for the proportion of animals that reached the adult stage. For survival, 35-40 L4 stage worms were incubated in each of three wells and transferred every two days to a fresh well for up to two weeks (thus ~100 worms were assayed in each experiment). Animals were examined every two days at the time of transfer, and inactive worms were scored as dead if they did not respond to repeated stimuli using a metal wire. Embryonic lethality was assayed by incubating 10 L4 worms to the adult stage and allowing adults lay eggs for 24h; mothers were then removed and the number of hatched versus unhatched eggs was counted 24h later (at which time all progeny would normally have hatched). To assay brood size, 10 L4 stage worms were incubated individually for two to three days, transferred to fresh wells, incubated for two more days, and the total number of progeny per adult worm counted.

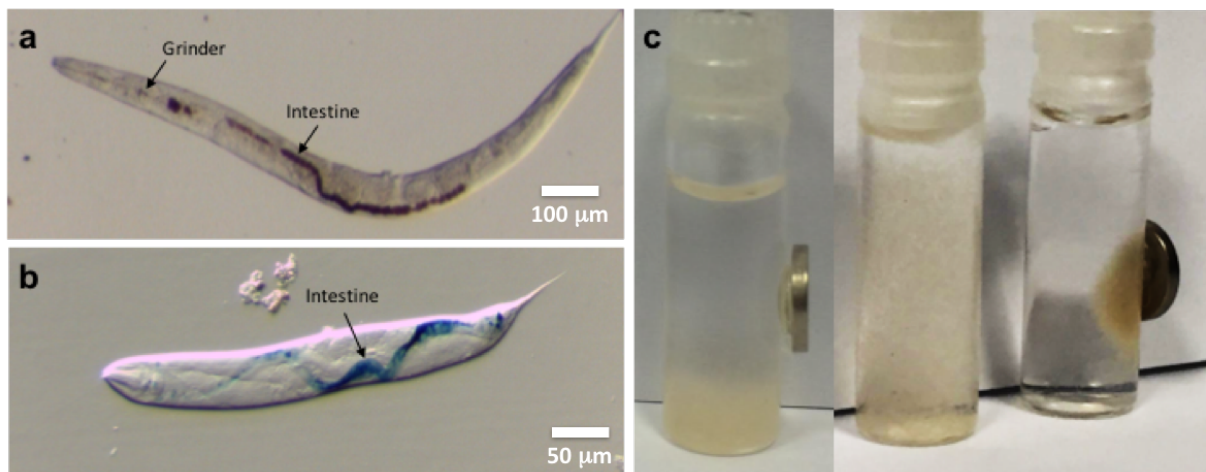


**Figure S22.** Intake of CB[7]NPs and worm magnetic behaviour (a) Nomarski image of a *C. elegans* nematode fed on CB[7]NP mixed with OP50 bacteria; arrows indicate the brown NP aggregates in the digestive system; (b) fixed *C. elegans* nematode stained with Prussian blue (iron stain) following CB[7]NP feeding; iron containing CB[7]NP are observed in the intestine; (c) mixed stage *C. elegans* fed on OP50 bacteria are not attracted to the magnet (left) and settle in the M9 solution; *C. elegans* nematodes fed with CB[7]NP and dispersed in M9 solution (middle) acquire a magnetic behaviour as they are attracted to the magnet attached to the tube (right).

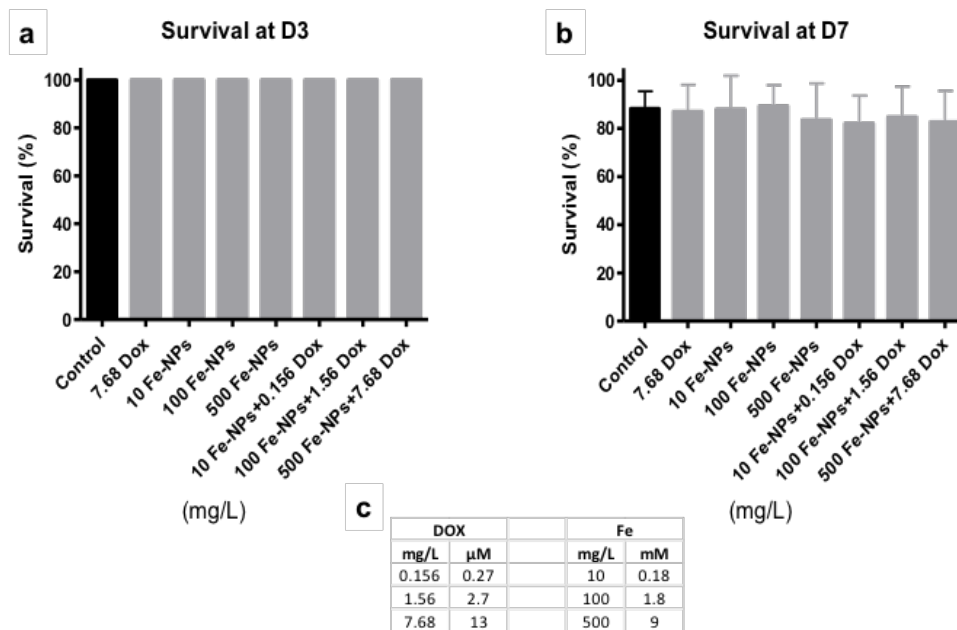


**Figure S23.** *C. elegans* adult nematodes survival after feeding on CB[7]NP or Dox@CB[7]NPs. L4 stage worms were incubated in presence of different concentrations of CB[7]NP or Dox@CB[7]NP and controls (OP50 and Dox); the survival of adults at day 3 (a) and day 7 (b) was not affected in the different conditions; the table (c) details the units conversion for the different concentrations tested. Bars represent standard error of the mean.

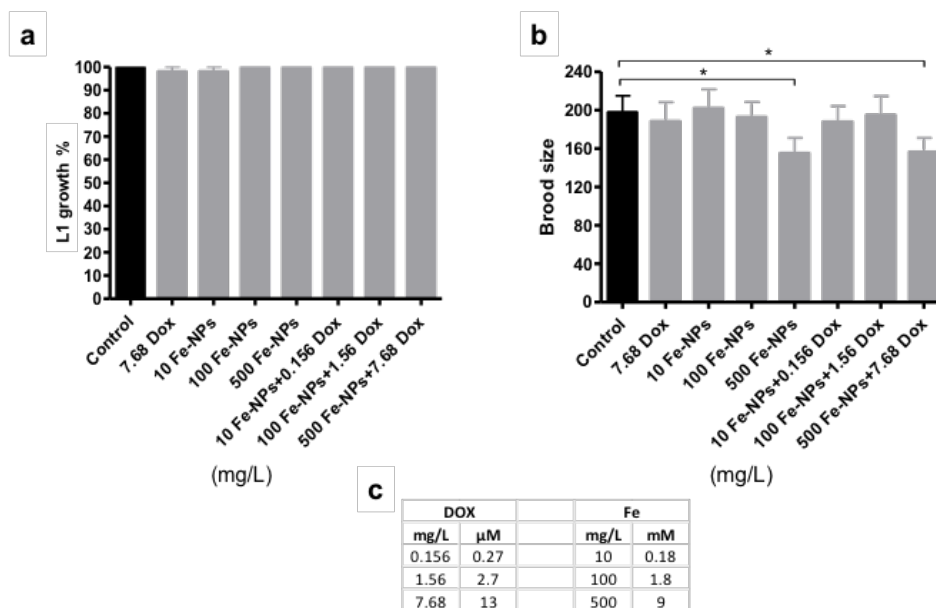


**Figure S24.** The effect of nanoparticles on L1 growth and brood size. (a) L1 stage worms were incubated in presence of different concentrations of CB[7]NP or Dox@CB[7]NP and controls (OP50 and Dox), and their growth rate to adult stage was not affected in the different conditions; (b) the brood size per individual adult worms was assessed in different conditions, and a significant reduction in brood size (~20%) was observed at the highest concentration (500 mg/L) of CB[7]NPs with or without doxorubicin; the table (c) details the units conversion for the different concentrations tested. Bars represent standard error of the mean. \*  $p < 0,05$ .

## 6. Computational studies

All calculations presented in this work were performed employing the Gaussian 09 package (Revision D.01).<sup>5</sup> Full geometry optimizations of the CB[7], Dox, CB[7]-Dox and CB[7]-GSH systems were carried out without any symmetry constraints using hybrid DFT with the B3LYP exchange-correlation functional<sup>6,7</sup> and the standard 6-31G(d,p) basis set. The X-ray structure of CB[7] was used as input geometry for structure optimization purposes,<sup>8</sup> while the input structures of Dox<sup>9</sup> was constructed taking into account previous conformational studies (**Figure S23**).

D-H...A	d(D-H)	d(H...A)	d(D...A)	<(DHA)
O1-H1A...O3	0.970	2.081	2.950	148.14
O1-H1B...O4	0.970	2.561	3.021	166.7
N1-H1C...O6	1.031	3.037	2.833	117.38
N1-H1D...O7	1.037	1.845	2.852	162.62
O2-H2...O5	0.974	1.857	2.772	120.99

**Table S3.** Hydrogen bonds (Å and degrees °) obtained from DFT calculations for the CB[7]-Dox system.

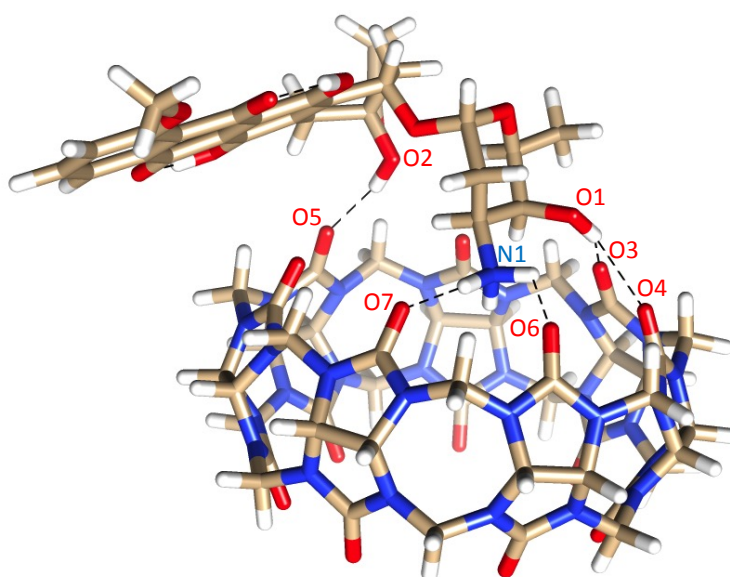
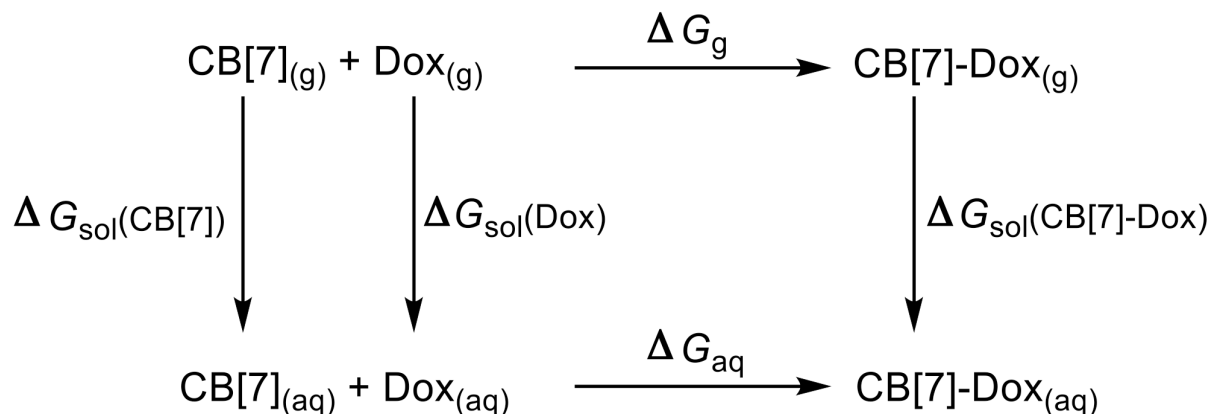


**Figure S25.** Hydrogen-bond interactions between the -NH<sub>3</sub> and -OH on the sugar ring of the DOX and the C=O groups on the rim of CB7.

The stationary points found on the potential energy surfaces as a result of the geometry optimizations have been tested to represent energy minima rather than saddle points via frequency analysis (0 imaginary frequencies). The Gibbs free energy of formation of the CB[7]-Dox adduct in water ( $\Delta G_{aq}$ ) was estimated by using the following thermodynamic cycle:



Where  $\Delta G_g$  is the Gibbs free energy of formation in the gas phase and  $\Delta G_{\text{sol}}$  are the hydration free energies of the different species. All the thermochemistry calculations were performed at standard conditions ( $T = 298.15 \text{ K}$  and  $P = 1 \text{ atm}$ ). Solvent effects (water) were evaluated by using the polarizable continuum model (PCM), in which the solute cavity is built as an envelope of spheres centered on atoms or atomic groups with appropriate radii. In particular, we used the integral equation formalism (IEFPCM)<sup>10</sup> variant as implemented in gaussian. The Gibbs free energy of formation of the CB[7]-Dox adduct was estimated to be  $-25.3 \text{ kJ mol}^{-1}$ , which points to a rather high stability of the supramolecular adduct.

### 7. Interaction of DOX with CB[7] in solution.

The interaction between Dox and CB[7] was monitored by titrating a solution of Dox in DMSO-d6 (1.2 mM) with a DMSO-d6 solution of CB[7] (0.012 M). Changes in the <sup>1</sup>H NMR spectral shifts of Dox are shown in the main text (**Figure S24**).

The assignment of the Dox <sup>1</sup>H NMR peaks are based on 2D NMR experiments and previously reported work.<sup>11</sup> The -OH and -NH<sub>3</sub> were distinguished based on the integration of each peak in DMSO-d6 as shown in the expanded region of the spectrum in **Figure S24**.

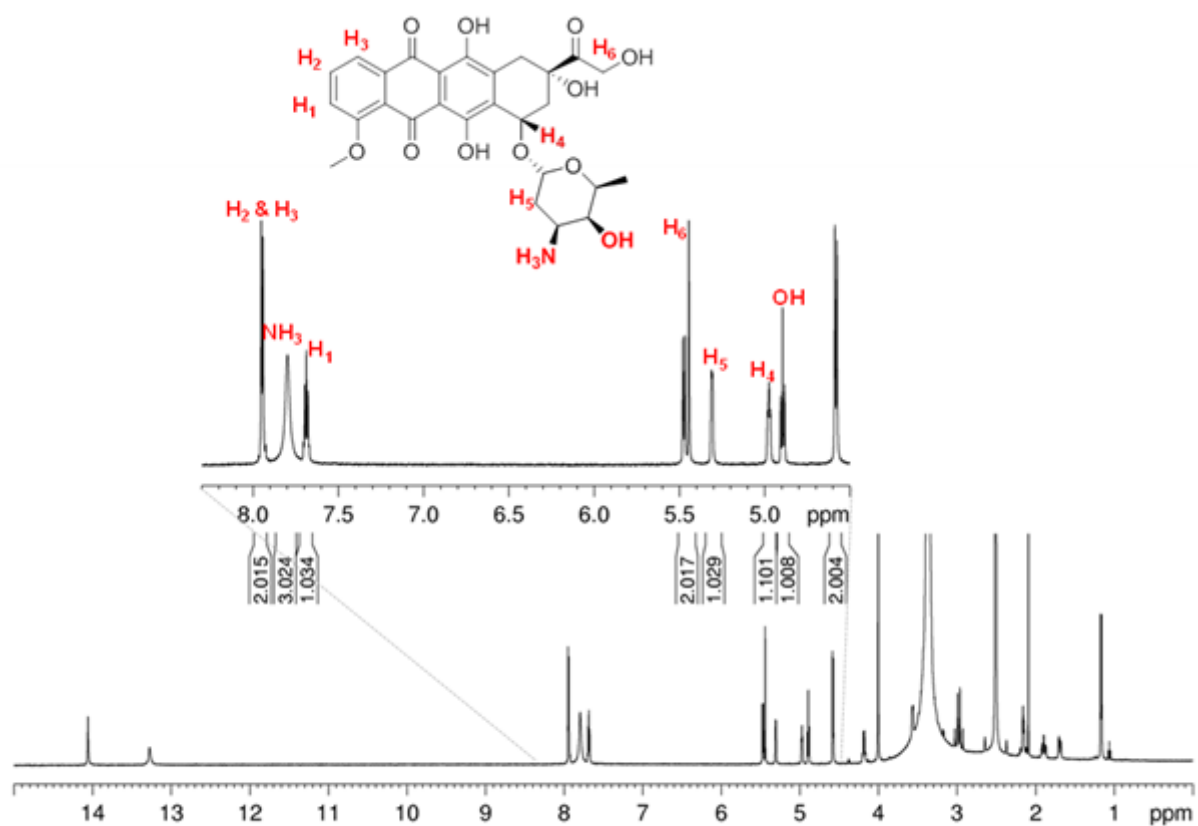


**Figure S26.** <sup>1</sup>H NMR spectrum of Dox (600 MHz, 298 K) in DMSO-d<sub>6</sub>.

## 8. Interaction of GSH with CB[7] in solution.

### 8.1. <sup>1</sup>H NMR spectroscopy

The interaction between GSH and CB[7] was also monitored by titrating a solution of GSH in D<sub>2</sub>O (1.39 mM) with a D<sub>2</sub>O solution of CB[7] (5.65 mM). Changes in the <sup>1</sup>H NMR chemical shifts of GSH are shown in **Figure S25**.

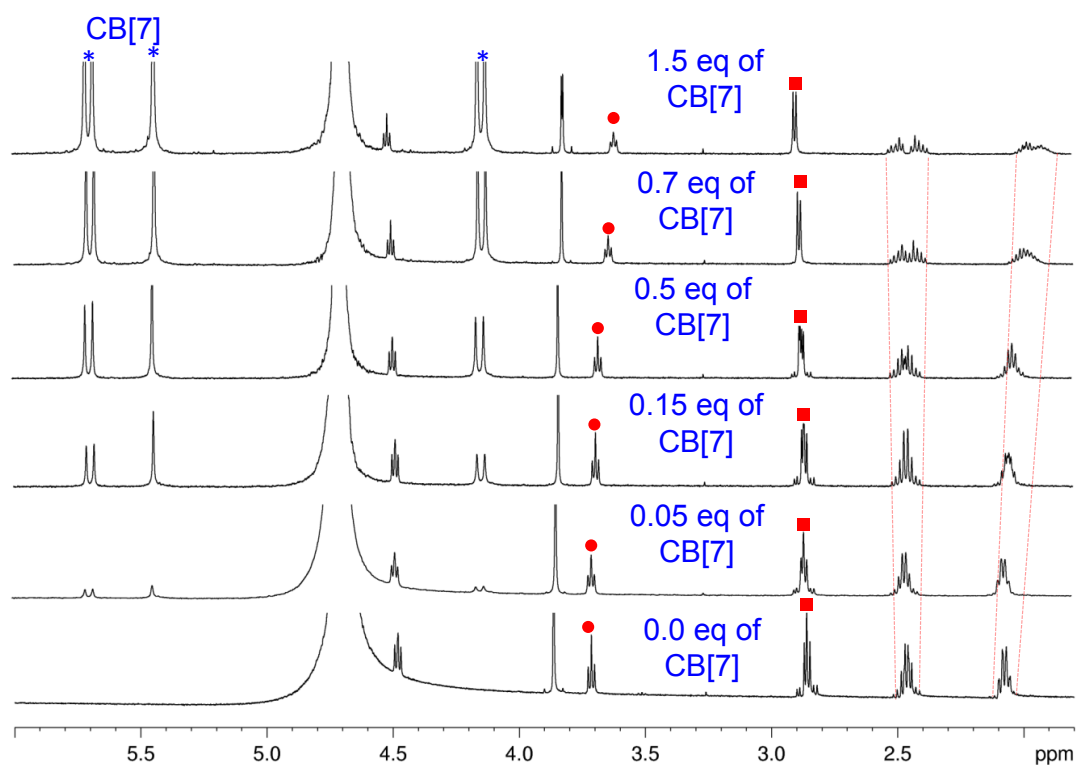


**Figure S27.** Changes in  $^1\text{H}$  NMR (600 MHz, 298 K) chemical shifts of GSH resulting from the titrating an aqueous solution of CB[7] to a solution of GSH in  $\text{D}_2\text{O}$ .

To evaluate the effects of deuterium/hydrogen exchange on Dox signal positions, a control experiment involving the titration of a DMSO solution of Dox with  $\text{D}_2\text{O}$  alone was also performed. The corresponding spectra (**Figure S26**) show that the  $\text{NH}_3^+$  peaks of Dox undergo a gradual downfield shift, and that they split. Also, the signal that corresponds to the hydroxyl group of the shifts upfield. In contrast, when Dox is titrated with CB[7] (Figure 1), the spectra show that the  $\text{NH}_3^+$  peaks are shifted upfield and that the hydroxyl proton signal stays in place and is broadened. These experiments indicate that the Dox signal shifts seen in DMSO with addition of a  $\text{D}_2\text{O}$  solution of CB[7] are due to an interaction between Dox and CB[7] and not to a deuterium/hydrogen exchange process.

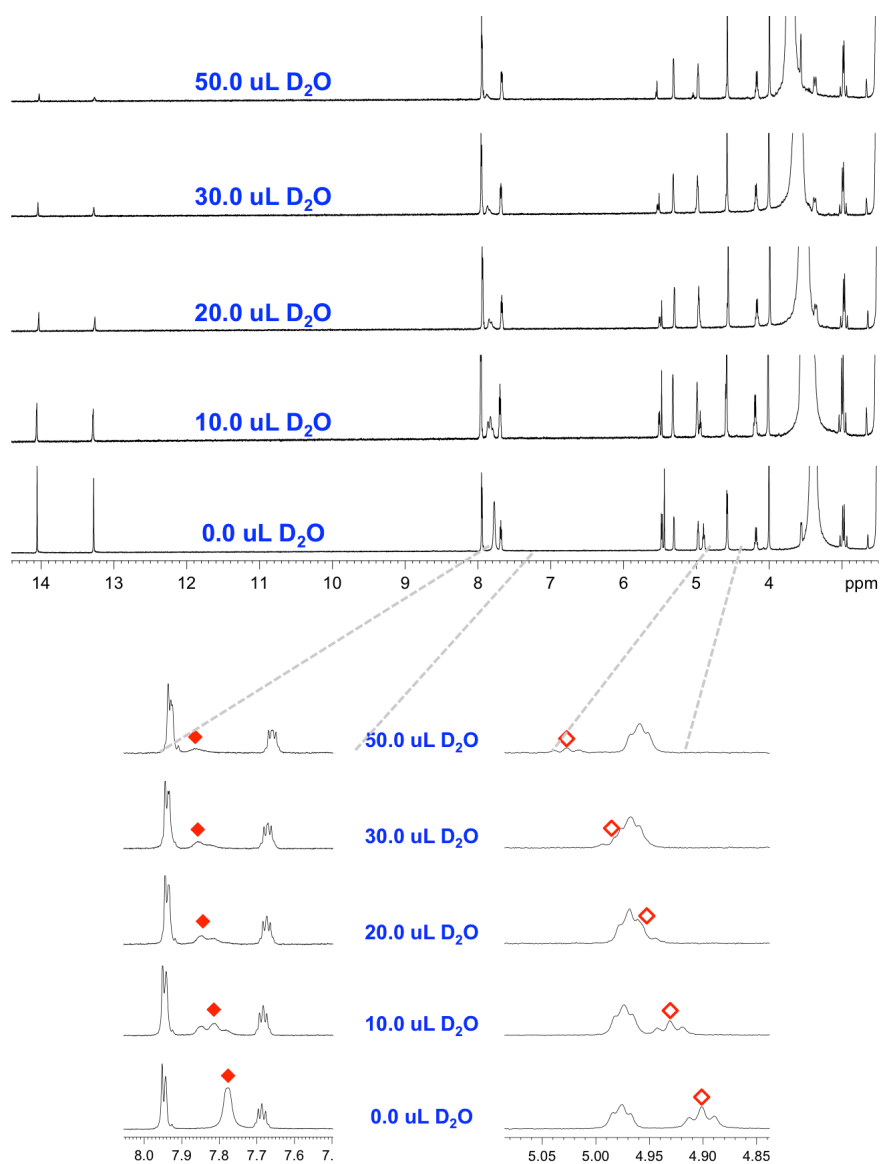


**Figure S28.**  $^1\text{H}$  NMR spectra (600 MHz, 298 K) illustrating changes in the chemical shifts of Dox signals that result from the titration of a solution of Dox (0.86 mM) in  $d_6$ -DMSO with increasing amounts of  $\text{D}_2\text{O}$ . The ammonium signal of Dox and the signal that corresponds to the hydroxyl proton of the Dox sugar moiety are labeled with filled and empty red rhombuses, respectively.

GSH was dissolved in a  $\text{D}_2\text{O}$  solution buffered with PBS. The  $^1\text{H}$  NMR spectra of GSH and GSH + CB[7] were recorded and are shown in **Figure S27**. The spectrum of GSH in the buffered solution is identical to the one acquired in  $\text{D}_2\text{O}$ . As for the spectral shifts of GSH upon the addition of CB[7], the same pattern of spectral shifts was observed in the buffer solution as was observed in unbuffered  $\text{D}_2\text{O}$ , but it seems that the binding strength is reduced slightly, where the spectral shift observed when introducing 1.5 eq. of CB[7] is observed upon the addition of 2.25 eq.

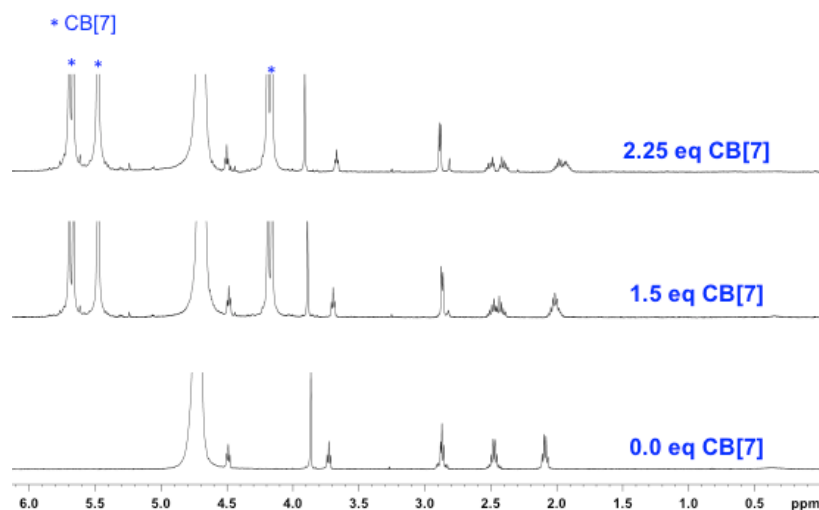


**Figure S29.** Stacked  $^1\text{H}$  NMR (600 MHz, 298 K) spectra corresponding to a titration of a buffered  $\text{D}_2\text{O}$  solution of GSH with increasing amounts of CB[7].

## 8.2. Isothermal Titration Calorimetry (ITC)

The complexation of GSH by CB[7] was investigated by ITC titration of a solution of CB[7] ( $7.5 \times 10^{-4}$  M) with a solution of GSH (0.038M) in water (**Figure S28**). The sample cell (0.2 mL) was filled with the CB[7] solution and the GSH solution was placed in a 40  $\mu\text{L}$  continuously stirred (1000 rpm) syringe. The injection sequence consisted of a first injection of 0.4  $\mu\text{L}$  of GSH that was discarded in the data analysis, to remove the effect of diffusion across the syringe tip during the equilibration period, followed by 36 injections of 1  $\mu\text{L}$  aliquots. The injections were separated by 150 s to ensure that the system reached equilibrium between two injections. The experiment was performed in triplicate from 3 different solutions of CB[7] and [GSH]. The heat of dilution of GSH in water and the heat of dilution of water in CB[7] were measured and subtracted from the heat of complexation before the fitting of the data.

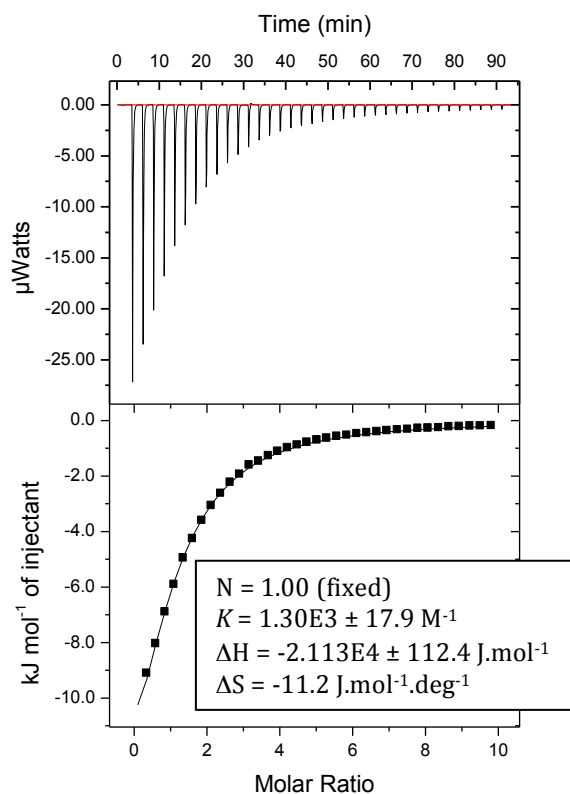


**Figure S30.** Heat effect and enthalpogram of the titration of CB[7] by GSH in water (corrected from dilutions effects).  $[CB[7]]_{tot} = 7.5 \times 10^{-4} \text{ M}$ ;  $0 < [GSH]/[CB[7]] < 9.81$ ; solvent: water;  $T = 298 \text{ K}$ .

Fitting of the data with a 1:1 model allowed us to calculate the stability of the (GSH)CB[7] complex of  $\log K = 3.16 \pm 0.05$ . Due to the shape of the titration, the value of  $\Delta H$  can only be extrapolated and is thus an estimation. The average of three independent titrations gave  $\Delta H = -21.0 \pm 0.8 \text{ kJ/mol}$  and a calculated value of  $-T\Delta S = 3 \pm 1 \text{ kJ/mol}$ . The enthalpically favorable association suggests good hydrogen bonding between GSH and CB[7] and the slightly positive value of  $-T\Delta S$  suggests minor unfavorable conformational changes and/or hydrophobic effect.

---

## . References

- (1) F. Benyettou, I. Milosevic, Y. Lalatonne, F. Warmont, R. Assah, J.-C. Olsen, M. Jouiad, L. Motte, C. Platas-Iglesias, A. Trabolsi, *J. Mater. Chem. B*, **2013**, *1*, 5076.
- (2) Geinguenaud, F.; Souissi, I.; Fagard, R.; Motte, L.; Lalatonne, Y. *Nanomedicine : nanotechnology, biology, and medicine* **2012**, *8*, 1106.
- (3) Brenner, S. The Genetics of CAENORHABDITIS ELEGANS. *Genetics* **1974**, *77*, 71-94.
- (4) Dawlatsina, G. I.; Minullina, R. T.; Fakhrullin, R. F. Microworms swallow the nanobait: the use of nanocoated microbial cells for the direct delivery of nanoparticles into *Caenorhabditis elegans*. *Nanoscale* **2013**, *5*, 11761-11769.
- (5) Gaussian 09, Revision A.01, Frisch, M. J.; Trucks, G. W.; Schlegel, H. B.; Scuseria, G. E.; Robb, M. A.; Cheeseman, J. R.; Scalmani, G.; Barone, V.; Mennucci, B.; Petersson, G. A.; Nakatsuji, H.; Caricato, M.; Li, X.; Hratchian, H. P.; Izmaylov, A. F.; Bloino, J.; Zheng, G.; Sonnenberg, J. L.; Hada, M.; Ehara, M.; Toyota, K.; Fukuda, R.; Hasegawa, J.; Ishida, M.; Nakajima, T.; Honda, Y.; Kitao, O.; Nakai, H.; Vreven, T.; Montgomery, Jr., J. A.; Peralta, J. E.; Ogliaro, F.; Bearpark, M.; Heyd, J. J.; Brothers, E.; Kudin, K. N.; Staroverov, V. N.; Kobayashi, R.; Normand, J.; Raghavachari, K.; Rendell, A.; Burant, J. C.; Iyengar, S. S.; Tomasi, J.; Cossi, M.; Rega, N.; Millam, N. J.; Klene, M.; Knox, J. E.; Cross, J. B.; Bakken, V.; Adamo, C.; Jaramillo, J.; Gomperts, R.; Stratmann, R. E.; Yazyev, O.; Austin, A. J.; Cammi, R.; Pomelli, C.; Ochterski, J. W.; Martin, R. L.; Morokuma, K.; Zakrzewski, V. G.; Voth, G. A.; Salvador, P.; Dannenberg, J. J.; Dapprich, S.; Daniels, A. D.; Farkas, Ö.; Foresman, J. B.; Ortiz, J. V.; Cioslowski, J.; Fox, D. J. Gaussian, Inc., Wallingford CT, 2009.
- (6) Becke, A. D. *J. Chem. Phys.* **1993**, *98*, 5648-5652.
- (7) Lee, C.; Yang, W.; Parr, R. G. *Phys. Rev. B* **1988**, *37*, 785-789.
- (8) Kim, J.; Jung, I.-S.; Kim, S.-Y.; Lee, E.; Kang, J.-K.; Sakamoto, S.; Yamaguchi, K.; Kim, K. *J. Am. Chem. Soc.* **2000**, *112*, 540-541.
- (9) a) Nakata, Y.; Hopfinger, A. J. *FEBS Lett.* **1980**, *117*, 259-264; b) Zhu, S.; Yan, L.; Ji, X.; Lu, W. *J. Mol. Struct. (Theochem)* **2010**, *951*, 60-68; c) Eswaramoorthy, S.; Kumaran, D.; Swaminathan, S. *Acta Cryst.* **2001**, *D57*, 1743-1746.
- (10) Tomasi, J.; Mennucci, B.; Cammi, R. *Chem. Rev.* **2005**, *105*, 2999-3093.
- <sup>11</sup> Ke, X.; Coady, D. J.; Yang, C.; Engler, A. C.; Hedrick, J. L.; Yang, Y. Y. *Polymer Chemistry* **2014**, *5*, 2621-2628.